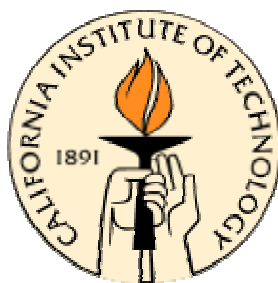


STUDIES with the AEROSOL MASS SPECTROMETER

Thesis by
Roya Bahreini

In Partial Fulfillment of the Requirements for the
Degree of Doctor of Philosophy



California Institute of Technology

Pasadena, California

2005

(Defended February 1, 2005)

Acknowledgements

Looking back at the years I spent at Caltech for my graduate studies, I feel privileged that I got the chance to meet and interact with many individuals whom I greatly respect for their scientific insights, and I am thankful for their invaluable support and friendship.

First, I thank Profs. John Seinfeld and Rick Flagan. I could not have completed this path without their continuous support, scientific insights, and patience throughout the years. They always kept me motivated and provided me with productive and useful advice when I needed guidance.

I have also interacted to a great extent with many people at Aerodyne Research, Inc. who have been involved with the Aerosol Mass Spectrometer. I am especially grateful to Doug Worsnop and John Jayne for their generous support and valuable technical and scientific insights and advice throughout the years.

My parents, sister, and uncle have always been a great support in my life, and the past few years at Caltech have not been an exception. Although we were usually hundreds of miles apart, I am very grateful for their continuous support and encouragement.

I have been very fortunate to be working in such a friendly and nice environment at Caltech, and I owe this to all the past and present members of Seinfeld/Flagan research group, especially the “Roofians”- Jose, David, Tomtor, Melita, Sally, Jesse, Dara, Song, and Jason. They not only made the experience in the lab pleasant, but also kept me good company when I needed to do something aside from being in the lab. I will always remember our mountain-watchings, endless afternoon snackings, and “eating-outings”!

During my Ph.D. study, I had the opportunity to participate in several field campaigns. I would like to thank the CIRPAS crew, especially Haf Jonsson, Roy Woods,

Nava Roy, Mike Hubble, and Reggie Burch, for making this experience as smooth as possible and for their support during the field studies. I share many good memories from these campaigns, thanks especially to Tomtor, Tracey, and Bill.

Although I have not worked as closely with Serena, Tim, Thanos and the rest of the members of our research group, I greatly value their friendship and appreciate their support during these years.

Many thanks to Ann Hilgenfeldt who has been so helpful and patient in accommodating me with what was needed for research in the lab and field projects. I would also like to thank Fran Matzen, Linda Scott, and Elizabeth Hinojos for their great administrative work. Thanks to Mike Vondrus and Suresh Guptha who always provided me their excellent expertise on usually rushed machining requests and panicking computer-related issues.

Finally, throughout my years at Caltech, I was lucky to meet my three very good friends—Mariu, Maca, and Pilar. Their support and friendship played a big role in making it easier for me to deal with the different issues throughout these years, and I am grateful for that. Thanks also to other friends that I met while at Caltech who kept me outside the lab when I needed a break. I enjoyed our gatherings, outdoor activities, parties, salsa classes, etc. to a great extent and have many good memories.

Abstract

Fast time-response of the Aerodyne Aerosol Mass Spectrometer (AMS) makes it a well-suited instrument for ambient field measurements. On the other hand, laboratory chamber experiments provide the opportunity to study a specific system in a more controlled environment. The goal of this thesis is to provide a summary of laboratory and field measurements using the AMS.

During laboratory chamber photooxidation experiments of diiodomethane (CH_2I_2), particle nucleation was observed at CH_2I_2 concentrations down to 15 ppt, which is comparable to the total gas-phase iodine species measured at coastal areas. Iodine oxides and oxyacids were observed in the aerosol mass spectra obtained by the AMS, consistent with the known gas-phase chemistry.

Airborne measurements by the AMS during the ACE-Asia field study revealed that the non-refractory submicron aerosols in the pollution layers of the boundary layer up to 3700 m were mainly composed of sulfate, ammonium, and organics. These pollution plumes originated primarily from urban and industrial areas of China and Korea.

The laboratory chamber experiments of oxidation of cycloalkenes, terpenes, and *m*-xylene provided the opportunity to study the Secondary Organic Aerosol (SOA) forming potential, i.e., yield, and determine SOA effective density and chemical composition. Evidence of acid-catalyzed heterogeneous chemistry in the ozonolysis of α -pinene was observed since the total AMS organic mass during the experiments with acidic seed particles had a greater contribution of higher molecular weight fragments. The mixtures of SOA compounds produced from similar precursors studied resulted in broadly similar

AMS mass spectra. Thus, fragmentation patterns observed for biogenic vs. anthropogenic SOA can be potentially useful in determining the sources of ambient SOA.

Table of Contents

Acknowledgement	iii
Abstract	v
List of Tables	xiv
List of Figures	xviii
1. Introduction	1
2. Marine Aerosol Formation from Biogenic Iodine Emissions	5
2.1. Abstract	6
2.2. Analysis	6
2.3. Methods	11
2.3.1. Laboratory Experiments	11
2.3.2. Aerosol Modeling	13
2.4. Acknowledgements	13
2.5. References	14
3. New Particle Formation from Photooxidation of Diiodomethane (CH_2I_2)	23
3.1. Abstract	24
3.2. Introduction	25
3.3. Experimental Description	28
3.3.1. CH_2I_2 (Surrogate) Concentration Measurement	29
3.3.2. Particle Number and Size Distribution Measurements	30
3.3.3. Aerosol Mass Spectrometer (AMS)	31
3.3.4. Hygroscopicity Tandem Differential Mobility Analyzer	32
3.3.5. Summary of Experiments Performed	32

3.4. Experimental Observations	33
3.4.1. Particle Formation and Growth	33
3.4.2. Hygroscopic Properties	38
3.4.3. Particle Composition	39
3.5. Interpretation of Size Distribution Observations	40
3.5.1. Estimates of Particle Effective Density	40
3.5.2. Estimation of Particle Fractal Dimension	46
3.6. Gas-Phase Chemistry and Aerosol Uptake Kinetic Simulations	51
3.6.1. Gas Phase Mechanism	51
3.6.2. Aerosol Uptake Modeling	54
3.6.3. Kinetic Simulations: Major Paths and Time Scale Analysis	56
3.6.4. Kinetic Simulations: Parametric Studies	59
3.6.5. Comparison of Experiments and Simulations	62
3.6.6. Kinetic Simulations: Results of the Alternative Mechanism Studies	63
3.7. Integrated Interpretation of the Aerosol Chemistry	67
3.8. Comparison to PARFORCE Results	73
3.9. Conclusions	76
3.10. Acknowledgements	77
3.11. References	77
4. Aircraft-Based Aerosol Size and Composition Measurements During ACE-Asia Using an Aerodyne Aerosol Mass Spectrometer	109
4.1. Abstract	110

4.2. Introduction	110
4.3. Aerodyne Aerosol Mass Spectrometer (AMS)	113
4.3.1 Instrument Description and Specifications	113
4.3.2. Fragmentation Patterns of Chemical Species in the AMS	115
4.3.3. Determination of Aerosol Chemical Composition	117
4.3.4. Detection Limits and Particle Statistics	119
4.3.5. Variation of the AMS Size Calibration with Sampling Altitude (Pressure)	121
4.3.6. Variation of the AMS Sample Flow Rate Measurement with Altitude	124
4.3.7. Variation of the AMS Internal Calibration Signal with Sampling Altitude (Pressure)	126
4.4. Results of Airborne Aerosol Size and Composition Measurements	127
4.4.1. Aerosol Species Mass Concentrations	127
4.4.2. Size-Resolved Aerosol Species Mass Distribution	130
4.5. Comparison of Twin Otter AMS and DMA Data	133
4.6. Comparison With Previous Measurements in the Region	136
4.7. Conclusions	141
4.8. Acknowledgements	141
4.9. References	142
5. Aerosol-Cloud Drop Concentration Closure in Warm Cumulus	172
5.1. Abstract	173
5.2. Introduction	174

5.3. Aerosol-CDNC Closure	176
5.4. Effects of Aerosol on the Vertical Profile of Cloud Microphysics	186
5.5. Relationships Among Hygroscopic Growth, CCN, and Organic Carbon	188
5.6. Discussion	194
5.7. Acknowledgements	198
5.8. References	198
6. Secondary Organic Aerosol Formation from Cyclohexene Ozonolysis: Effect of OH Scavenger and the Role of Radical Chemistry	216
6.1. Abstract	217
6.2. Introduction	217
6.3. Experimental Methods	219
6.4. Experimental Results	220
6.5. Scavenger Chemistry	222
6.6. Mechanism Description	224
6.7. Mechanism Predictions	227
6.8. Implications	231
6.9. Acknowledgements	234
6.10. References	234
7. Secondary Organic Aerosol Formation from the Ozonolysis of Cycloalkenes and Related Compounds	252
7.1. Abstract	253
7.2. Introduction	253

8.4.2.2. Identification and Structure Elucidation of Oligomers in SOA	301
8.4.2.3. Assessing Relative Abundance of Oligomers in SOA	304
8.4.3. Relationship Between HC Precursor Structure and SOA Composition and Yield	305
8.4.3.1. Carbon Number in Homologous Cycloalkenes	306
8.4.3.2. Methyl-Substitution Effect	307
8.4.3.3. Isomeric Effect	308
8.5. Conclusions	310
8.6. Acknowledgements	311
8.7. References	312
9. Particle Phase Acidity and Oligomer Formation in Secondary Organic Aerosol	342
9.1. Abstract	343
9.2. Introduction	343
9.3. Experimental	345
9.4. Results and Discussion	347
9.5. Acknowledgements	351
9.6. References	352
10. Measurements of Secondary Organic Aerosol (SOA) from oxidation of cycloalkenes, terpenes, and <i>m</i> -xylene using an Aerodyne Aerosol Mass Spectrometer	362

10.1. Abstract	363
10.2. Introduction	364
10.3. Experimental	366
10.4. Determination of SOA Density and Morphology	369
10.5. Analysis of Organics	372
10.6. Results and Discussion	373
10.6.1. Dark Ozonolysis of Cycloalkene Precursors	373
10.6.2. Dark Ozonolysis of Biogenic Precursors	375
10.6.3. Photooxidation of <i>m</i> -xylene	381
10.7. Common Features in Different Systems	382
10.8. Acknowledgements	384
10.9. References	385
11. Appendix A: Supplementary Material for “Secondary Organic Aerosol Formation from the Ozonolysis of Cycloalkenes and Related Compounds”	419
12. Appendix B: Supplementary Material for “Low-Molecular-Weight and Oligomeric Components in Secondary Organic Aerosol from the Ozonolysis of Cycloalkenes and α -pinene”	428
13. Appendix C: Supplementary Material for “Particle Phase Acidity and Oligomer Formation in Secondary Organic”	434
14. Summary	444

List of Tables

Table 3.1. Summary of the experiments performed	86
Table 3.2. Chemical mechanism used in the gas-phase and aerosol uptake simulations	87
Table 3.3. Summary of chemical kinetics simulations performed as direct comparison to the experiments and as parametric studies of the base case	89
Table 3.4. Summary of chemical kinetics simulations performed as tests of alternative mechanisms for the gas-phase chemical kinetics, different aerosol uptake parameters, or with solar light instead of chamber light (black-lights)	90
Table 3.5. Summary of the effects of variations of the rates and structure of the kinetic mechanism on the agreement between experiments and simulations, and on the major predicted aerosol species	91
Table 3.6. Synthesis of evidence on aerosol composition and identity of nucleating species	92
Table 4.1. Typical measured (1-minute) and estimated (longer times) AMS detection limits for sulfate, nitrate, ammonium, and organics during ACE-Asia	146
Table 4.2. Typical operational parameters used and examples of particle counting statistics during ACE-Asia	147
Table 4.3 Constant altitude legs of Twin Otter flights	148
Table 4.4. AMS averaged mass concentration data ($\mu\text{g m}^{-3}$ at STP) and standard deviations (STD, $\mu\text{g m}^{-3}$ at STP) of sulfate, nitrate, and ammonium during constant-altitude legs	149

Table 4.5. AMS sulfate, organics, nitrate, and ammonium mass distribution vacuum aerodynamic mode diameter (nm) and Full Width Half Maximum (FWHM, nm) measured during constant-altitude-legs	150
Table 4.6. Ratio of the AMS total mass concentration to DMA volume concentration and estimated density	151
Table 4.7. Average aerosol concentrations in April at Cheju Island during 1992-1995	152
Table 4.8. Summary of AMS measurements of sulfate, nitrate, organics, and ammonium mass concentrations and the corresponding molar and mass ratios at different altitudes	153
Table 5.1. Aerosol, cloud and meteorological instrumentation for ONR's CIRPAS Twin Otter aircraft during CRYSTAL-FACE	204
Table 5.2. Summary of cloud observations	205
Table 5.3. Effects of changing model assumptions on predicted CCN and CDNC	206
Table 6.1. Initial conditions and data for cyclohexene ozonolysis reactions	237
Table 6.2. Reactions and rate constants used in the mechanism	238
Table 6.3. Branching ratios used in the mechanism	239
Table 7.1. Parent hydrocarbons	271
Table 7.2. Initial conditions and data for alkene ozonolysis experiments	272
Table 7.3. Aerosol yield parameters for the ozonolysis of cycloalkenes and related compounds	274
Table 7.4. Matrix of correlation coefficients	275
Table 7.5. Results of principal component analysis	275

Table 8.1. Molecular structures of precursor hydrocarbons investigated in this study	314
Table 8.2. Low-MW components in SOA from cyclopentene ozonolysis	315
Table 8.3. Low-MW components in SOA from cyclohexene ozonolysis	317
Table 8.4. Low-MW components in SOA from cycloheptene ozonolysis	318
Table 8.5. Low-MW components in SOA from 1-methyl cyclopentene ozonolysis ...	320
Table 8.6. Low-MW components in SOA from 1-methyl cyclohexene ozonolysis	321
Table 8.7. Low-MW components in SOA from 3-methyl cyclohexene ozonolysis	323
Table 8.8. Mass percentage of each class of compounds in the total identified low-MW SOA species in six ozonolysis systems	325
Table 8.9: Fraction of each class of compounds in the total SOA mass derived from the DMA measurements (first four rows). Fractions of identified low-MW species (no oxalic acid) in the total SOA mass (5 th row). Fractions of the identified low-MW species (including the estimated oxalic acid) in the total SOA mass (6 th row). Fractions of the total identified species, both low-MW and oligomeric, in the total SOA mass (7 th row)	326
Table 8.10: Structures illustrating the numbers of available α -C and α -H for aldol reactions in some initial oxidation products in 1-methyl cyclohexene, cycloheptene, and 3-methyl cyclohexene ozonolysis systems	328
Table 10.1. Summary of conducted experiments	392
Table 10.2. Estimated effective density of SOA during cycloalkene ozonolysis experiments in the presence or absence of seed aerosol	394
Table 10.3. Estimated effective density of SOA during biogenic ozonolysis	

experiments	394
Table 10.4. Estimated pH values of seed particles and their relative bulk concentrations	394
Table 10.5. Relative contribution of different fragments to total organic signal	395
Table B.1. Standard compounds calibrated, m/z of molecular ions [M-1], and average and standard deviation of retention times	429
Table B.2. Molecular structures and molecular weights of identified low-MW components in SOA from the ozonolysis of cycloalkenes	430

List of Figures

Figure 2.1. Observed aerosol mass spectrum from chamber experiments as measured by the AMS	18
Figure 2.2. Chemical pathway from CH_2I_2 to aerosol production based on the current state of knowledge of the gas phase chemistry	19
Figure 2.3. Model simulations of condensable vapor and aerosol concentrations in the marine boundary layer	20
Figure 2.4. Predicted aerosol size distributions before (06:00 hours), during (14:00 hours) and after (20:00 hours) the particle production period with CIV source rates (Q) of 0, 10^3 , 5×10^3 , 10^4 and 2.5×10^4 molecules $\text{cm}^{-3} \text{s}^{-1}$	22
Figure 3.1. Evolution of the number, volume, and mass concentrations in the chamber as a function of time after inception of photolysis for the base case experiment	93
Figure 3.2. Evolution of the number, volume, and mass concentrations in the chamber during the initial minutes after inception of photolysis for the base case experiment	94
Figure 3.3. SEMS Size distributions at different times during the base case experiment	95
Figure 3.4. Comparison of the volume size distributions measured by the SEMS with the mass distributions measured by the AMS for two times during the base case experiment	96

Figure 3.5. Comparison of the maximum experimental particle number, area, and volume concentrations measured in the chamber as a function of initial CH ₂ I ₂ mixing ratio	97
Figure 3.6. Observed time scales of gas-to-particle conversion as a function of initial CH ₂ I ₂ mixing ratio	98
Figure 3.7. Hygroscopic growth factor determined by the Hygroscopicity Tandem Differential Mobility Analyzer (HTDMA) as a function of relative humidity for experiments E1 and E2	99
Figure 3.8. Total aerosol mass spectrum measured with the Aerodyne AMS for experiment E6	100
Figure 3.9. Calculated variation of the mobility diameter, vacuum aerodynamic diameter, and effective density	101
Figure 3.10. Comparison of the measured size distributions during the base case experiment	102
Figure 3.11. Theoretical decay of particle number concentrations as a function of the mass fractal dimension	103
Figure 3.12. Schematic representation of the chemical mechanism used in the gas-phase and aerosol uptake simulations	104
Figure 3.13. Simulated concentration profiles of the main iodine species for the simulation base case S1	105
Figure 3.14. Mixing ratios (i.e., mole fraction) of the aerosol species predicted by the simulation mechanism as a function of initial CH ₂ I ₂ concentration	106
Figure 3.15. Comparison of the observed and predicted O ₃ concentrations	

evolutions	107
Figure 3.16. Predicted gas-phase concentrations at the inception of the experimental nucleation burst	108
Figure 4.1. Twin Otter flight tracks during ACE-Asia for the flights in which the AMS obtained valid data	154
Figure 4.2. Schematic diagram of the Aerodyne Aerosol Mass Spectrometer	155
Figure 4.3. Variation of the pressure inside the aerodynamic lens in the AMS inlet with sampling pressure	156
Figure 4.4. Particle velocity (a) and time of flight (b) variation with ambient pressure for different particle vacuum aerodynamic diameters	157
Figure 4.5. Variation of air beam signal intensity ($m/z=32, O_2^+$) with ambient pressure	158
Figure 4.6. Concentration profiles of sulfate (a), organics (a), nitrate (b), and ammonium (b) for Twin Otter RF17	159
Figure 4.7. Concentration profiles of sulfate (a) and organics (b) for Twin Otter RF9, RF11, and RF17	160
Figure 4.8. Time trend of total sulfate concentration and the size-resolved mass distribution of this species during Twin Otter RF9	162
Figure 4.9. Pie-chart representation of major organic fragments and their contribution (as a percentage) to the total estimated organics mass concentration	163
Figure 4.10. Average ammonium and sulfate mass distributions during Twin Otter RF17	164

Figure 4.11. Average mass distributions of ammonium, sulfate, and nitrate during Twin Otter RF17	165
Figure 4.12. Average mass distribution for species with fragments at $m/z=44$ amu during Twin Otter RF17	166
Figure 4.13. Average sulfate mass distributions scaled to maximum for Twin Otter RF9	167
Figure 4.14. Average sulfate and ammonium mass distributions for marine boundary layer (a and c) and pollution layers (b and d) on Twin Otter RF9, RF11, and RF17	168
Figure 4.15. Time trend of the AMS total mass concentration and DMA total dry aerosol volume concentration on Twin Otter RF17 (a) and the linear fit to the data (b)	170
Figure 4.16. Comparison of AMS average mass distribution of sulfate and organics and DMA average total dry aerosol volume distribution on RF17	171
Figure 5.1. Map of the CRYSTAL-FACE region in S. Florida. Each symbol denotes the location of a cloud characterized by the Twin Otter	207
Figure 5.2. Aerosol-CDNC closure. Predicted vs. observed droplet concentration	208
Figure 5.3. CCN-forced variations in CDNC and influence on the vertical profile of effective radius	209
Figure 5.4. Illustration of methods 1 and 2 for determining hygroscopic growth factor from the DACADS data	210

Figure 5.5. A) Effective cutoff diameter for $S_C=0.85\%$ plotted vs. $f(\text{RH})$ for the Aitken mode using Method 2. B) $f(\text{RH})$ plotted vs. humid DMA RH for the same points as in Figure 5.5A	211
Figure 5.6. Percent difference between observed CCN(0.85%) and $N(d > 32 \text{ nm})$ obtained from the DMA plotted as a function of $f(\text{RH})$ of the Aitken mode	213
Figure 5.7. Relationship between $D_C(0.85\%)$ and AMS measured organic carbon to sulfate mass ratio	214
Figure 5.8. A) Relationship between Aitken mode $f(\text{RH})$ and AMS measured organic carbon to sulfate mass ratio for $\text{OC}:\text{SO}_4^{2-}$ ratios below 0.5. B) Same as A, but for accumulation mode $f(\text{RH})$	215
Figure 6.1. Initial steps of the cyclohexene-ozone reaction	240
Figure 6.2. SOA yield for ozonolysis of cyclohexene in the presence of different OH scavengers	241
Figure 6.3. SOA yield for ozonolysis of cyclohexene in the presence of 2-butanol at differing temperatures	242
Figure 6.4. Relationship between temperature and deviation in yield from the fitted yield curve for cyclohexane and 2-butanol scavenger experiments	243
Figure 6.5. SOA yield curves for ozonolysis of cyclohexene in the presence of 2-butanol scavenger and cyclohexane scavengers	244
Figure 6.6. The three classes of organic peroxy radicals modeled in this study: (a) RO_2 , the peroxy radical co-generated with OH in the ozonolysis reaction; (b) $\text{R}^{\text{S}}\text{O}_2$,	

from reaction with the cyclohexane 2-butanol scavengers; and (c) AcylO ₂ , acylperoxy radicals	245
Figure 6.7. Possible reaction pathways of the RO radical generated in the self-reaction of RO ₂	246
Figure 6.8. Predicted and measured ozone and cyclohexene concentrations for a typical experiment	247
Figure 6.9. Predicted radical concentrations for ozonolysis of 200 ppb of cyclohexene for each of the three scavengers used: (a) CO; (b) 2-butanol; and (c) cyclohexane	248
Figure 6.10. Predicted organic acid (including peracid) concentrations for each scavenger, from the ozonolysis of 200 ppb of cyclohexene, assuming no acyl radicals are formed directly by the ozonolysis reaction	250
Figure 6.11. Predicted organic acid (including peracid) concentrations for each scavenger, for the ozonolysis of 200 ppb cyclohexene, assuming an acyl radical yield of 0.05 from the ozonolysis reaction	251
Figure 7.1. Structure of parent hydrocarbons investigated in this study	276
Figure 7.2. SOA yield data and curves fitted by Equation 1 as a function of ΔM_o for the cycloalkenes	277
Figure 7.3. SOA yield data and curves fitted by Equation 1 as a function of ΔM_o for (a) cyclopentene and 1-methyl-1-cyclopentene, (b) cyclohexene and 1-methyl-1- cyclohexene, and (c) cycloheptene and 1-methyl-1-cycloheptene	278

Figure 7.4. Yield SOA yield data and curves fitted by Equation 1 as a function of ΔM_o for (a) cyclohexene and 1-methyl-1-cyclopentene, (b) cycloheptene and 1-methyl- 1-cyclohexene and, (c) cyclooctene and 1-methyl-1-cycloheptene	280
Figure 7.5. SOA yield data and curves fitted by Equation 1 as a function of ΔM_o for cyclohexene, 1-methyl-1-cyclohexene and 3-methyl-1-cyclohexene	282
Figure 7.6. SOA yield data and curves fitted by Equation 1 as a function of ΔM_o for terpinolene relative to cyclohexene, 1-methyl-1-cyclohexene and methylene cyclohexane	283
Figure 7.7. Initial ozone reactions with the main cycloalkene structures to form Criegee intermediates	284
Figure 8.1. Typical total ion chromatograms of SOA from the ozonolysis of cycloalkenes	329
Figure 8.2. Total ion chromatograms (TIC) and extracted ion chromatograms (EIC) of 145, 185, and 243 ions of SOA from cycloheptene ozonolysis	330
Figure 8.3. Late-eluting chromatographic peaks in SOA from cycloalkene ozonolysis	331
Figure 8.4. Ion trap mass spectrum (- ion mode) of SOA from cycloheptene Ozonolysis	332
Figure 8.5. Ion trap mass spectrum (- ion mode) of SOA from 1-methyl cyclopentene ozonolysis	333
Figure 8.6. (a) Ion trap mass spectrum (- ion mode) of SOA from α -pinene ozonolysis with pre-existing $MgSO_4$ seed particles; (b) Ion trap mass spectrum (+ ion mode) of the same SOA as in (a)	334

Figure 8.7. MS/MS (- ion mode) of 373 ion in the SOA from cycloheptene ozonolysis, as shown in Figure 8.4	336
Figure 8.8. (a) Ion trap mass spectrum (+ ion mode) of the SOA from the ozonolysis of 120 ppb α -pinene on MgSO_4 -only seed; (b) Ion trap mass spectrum (+ ion mode) of the SOA from the ozonolysis of 120 ppb α -pinene on MgSO_4 - H_2SO_4 seed	337
Figure 8.9. The absolute yields of SOA formed on nonacid (dotted bars) and acid (lined bars) MgSO_4 seed particles at seven initial α -pinene mixing ratios	339
Figure 8.10. The extracted ion chromatograms of 289 ion in SOA from the ozonolysis of 1-methyl cyclohexene, cycloheptene, and 3-methyl cyclohexene	341
Figure 9.1. The relative yield difference (RYD) of SOA between the acid and nonacid cases for seven pairs of α -pinene ozonolysis experiments on MgSO_4 seeds, two pairs on $(\text{NH}_4)_2\text{SO}_4$ seeds, as well as two pairs of terpinolene ozonolysis experiments on MgSO_4 seeds	354
Figure 9.2. Ion trap mass spectrum (+ ion mode) of the extract of SOA from the ozonolysis of (a) 120 ppb α -pinene on MgSO_4 -only seed (RH = 55%); (b) 120 ppb α -pinene on MgSO_4 - H_2SO_4 seed; (c) 72 ppb α -pinene on $(\text{NH}_4)_2\text{SO}_4$ -only seed; (d) 72 ppb α -pinene on $(\text{NH}_4)_2\text{SO}_4$ - H_2SO_4 seed.	355
Figure 9.3. MS/MS (- ion mode) of (a) 357 ion in the SOA from the same α -pinene ozonolysis experiment; (b) 245 ion in the SOA from 1-methyl cyclopentene ozonolysis	358
Figure 9.4. Ion trap mass spectrum (+ ion mode) of the extract of SOA from the ozonolysis of 180ppb α -pinene in the presence of dry $(\text{NH}_4)_2\text{SO}_4$ -only	

seed	360
Figure 9.5. Ion trap mass spectrum (+ ion mode) of the extract of SOA from the ozonolysis of 50ppb α -pinene in the absence of seed particles	361
Figure 10.1. Chemical structures of the SOA precursor compounds studied	396
Figure 10.2. Comparison of AMS and DMA mass distributions as a means to deduce aerosol effective density	397
Figure 10.3. Evolution of mass distributions of organics and sulfate (a-c) and the mass spectra (d-e) during cyclohexene ozonolysis	399
Figure 10.4. Time trends of sulfate and organic mass concentrations during cyclopentene ozonolysis	402
Figure 10.5. Fraction of the organic signal at $\Delta=4$ (common Δ group for $C_nH_{2n-1}O_2^+$ fragment of acids) and m/z 44 (CO_2^+ fragment of acids) in total SOA mass during initial stages of cycloheptene oxidation	403
Figure 10.6. Ion trap mass spectra of SOA from α -pinene (100 ppb) ozonolysis; (a) in the presence of $MgSO_4$ seed particles; (b) in the absence of any seed particles	404
Figure 10.7. Relationship between SOA effective density with relative contribution of m/z 44 signal to total organic signal for different classes of parent hydrocarbons	406
Figure 10.8. Time trends of sulfate and organic mass concentrations in ozonolysis of linalool	407
Figure 10.9. Average delta values of different size fragments for anthropogenic and biogenic SOA	408

Figure 10.10. Relative contribution of higher molecular weight fragments to total organic mass during ozonolysis of α -pinene in the presence of different seed particles	409
Figure 10.11. (a) Relative contribution of different Δ groups to total SOA mass formed from ozonolysis of α -pinene in the presence of MgSO_4 or $\text{MgSO}_4+\text{H}_2\text{SO}_4$ seed aerosols; (b) Fraction of organic signal due to m/z 44 and $\Delta=3$ during ozonolysis of α -pinene in the presence of MgSO_4 or $\text{MgSO}_4+\text{H}_2\text{SO}_4$ seed	410
Figure 10.12. (a) Relative contribution of different Δ groups to total SOA mass formed from photooxidation of m -xylene in the presence of $(\text{NH}_4)_2\text{SO}_4$ or $(\text{NH}_4)_2\text{SO}_4 + \text{H}_2\text{SO}_4$ seed aerosols; (b) Fraction of organic signal due to m/z 44 and $\Delta=3$ during photooxidation of m -xylene in the presence of $(\text{NH}_4)_2\text{SO}_4$ or $(\text{NH}_4)_2\text{SO}_4 + \text{H}_2\text{SO}_4$ seed aerosols	412
Figure 10.13. Time trend of main fragments of 2,5-furandione (m/z 54), 3-methyl-2,5-furandione (m/z 68), and nitrate (m/z 30 and 46) during photooxidation of m -xylene	414
Figure 10.14. Mass spectra of SOA formed during α -pinene, m -xylene, and cyclopentene oxidation experiments as well as ambient organic mass spectra of Ohio background pollution, Cleveland, OH pollution, and brush fire plumes	415
Figure 10.15. Delta analysis of mass spectra obtained from brush fire, Cleveland, and background Ohio pollution plumes	416

Figure 10.16. Average delta values of different size fragments of ambient organic mass spectra obtained in brush fire, Cleveland pollution, and background Ohio pollution plumes	418
Figure A.1. Time series for ozone, hydrocarbon and particle volume concentration for each compound measured in this study.....	423
Figure A.2. Rate of hydrocarbon consumption as a function of hydrocarbon concentration	424
Figure A.3. Rate of hydrocarbon consumption as a function of k_{O_3} based upon an initial hydrocarbon concentration of 200 ppb	425
Figure A.4. Time for the onset of particle growth as a function of k_{O_3}	426
Figure A.5. Rate of particle growth as a function of hydrocarbon concentration	427
Figure C.1. The extracted ion chromatograms of 185, 171, 199 and 183 ions detected by the LC-MS in the SOA from the same α -pinene ozonolysis experiment as shown in Figures 9.2(a) and 9.3(a)	435
Figure C.2. Ion trap mass spectrum (- ion mode) of the extract of SOA from the same α -pinene ozonolysis experiment as shown in Figures 9.2(a) and 9.3(a)	437
Figure C.3. Ion trap mass spectrum (+ ion mode) of the extract of a typical blank filter serving as the background MS	439
Figure C.4. Ion trap mass spectra (+ ion mode) of the extracts of SOA from another pair of α -pinene (96 ppb) ozonolysis experiments: (a) on $MgSO_4$ -only seed; (b) on $MgSO_4$ - H_2SO_4 seed	440
Figure C.5. The likely structures of 313, 171 and 185 fragment ions in Figure 9.3(a)	442

Figure C.6. Ion trap mass spectrum (- ion mode) of the extract of SOA from the
ozonolysis of 184ppb cycloheptene on dry $(\text{NH}_4)_2\text{SO}_4$ seed 443